DTU Library

Gaining Insight into the Electrochemical Interface Dynamics in an Organic Redox Flow Battery with a Kinetic Monte Carlo Approach

Yu, Jia; Shukla, Garima; Fornari, Rocco Peter; Arcelus, Oier; Shodiev, Abbos; de Silva, Piotr; Franco, Alejandro A.

[Link back to DTU Orbit](#)

Gaining Insight into the Electrochemical Interface Dynamics in an Organic Redox Flow Battery with a Kinetic Monte Carlo Approach

Jia Yu, Garima Shukla, Rocco Peter Fornari, Oier Arcelus, Abbos Shodiev, Piotr de Silva, and Alejandro A. Franco*

Finding low-cost and nontoxic redox couples for organic redox flow batteries is challenging due to unrevealed reaction mechanisms and side reactions. In this study, a 3D kinetic Monte Carlo model to study the electrode-anolyte interface of a methyl viologen-based organic redox flow battery is presented. This model captures various electrode processes, such as ionic displacement and degradation of active materials. The workflow consists of input parameters obtained from density functional theory calculations, a kinetic Monte Carlo algorithm to simulate the discharging process, and an electric double layer model to account for the electric field distribution near the electrode surface. Galvanostatic discharge is simulated at different anolyte concentrations and input current densities, which demonstrate that the model captured the formation of the electrical double layer due to ionic transport. The simulated electrochemical kinetics (potential, charge density) are found to be in agreement with the Nernst equation and the obtained EDL structure corresponded with published molecular dynamics results. The model's flexibility allows further applications of simulating the behavior of different redox couples and makes it possible to consider other molecular-scale phenomena. This study paves the way for computational screening of active species by assessing their potential kinetics in electrochemical environments.

1. Introduction

Storing electricity at off-peak hours to feed the power grid at on-peak hours is a fundamental problem for the renewable energy field. The available solution is developing an efficient, economical, and environmentally friendly large-scale energy storage device to balance the production and demand of electricity. The redox flow battery (RFB) system is a promising candidate among all the energy storage devices due to its relatively low cost, high energy efficiency, and feasibility for large-scale energy storage applications.

To date, vanadium-based redox flow batteries (VRFB) are among the most reliable RFB technologies due to their limited cross-contamination effect and relatively large power output. Moreover, the electrolyte of a VRFB shows limited aging, which is the main reason for its high capacity retention rate.[1,2] However, compared with the E.U. cost target (150 € kW h^{-1}),[3] a VRFB system remains relatively expensive (≈400 € kW h^{-1} for 2 kW-class facilities)[4,5] due to the cost of the ion exchange membrane and raw materials. Meanwhile, vanadium mining and production lead to soil pollution and a toxic impact on plants, animals, and humans around the mining sites.[6] Therefore, organic redox flow batteries (ORFBs) have attracted much attention due to the significantly faster redox kinetics, the ability to tune electrochemical properties through organic synthesis, and the low

J. Yu, G. Shukla, O. Arcelus, A. Shodiev, A. A. Franco
Laboratoire de Réactivité et Chimie des Solides (LRCS)
UMR CNRS 7314
Université de Picardie Jules Verne
Hub de l'Energie
15 rue Baudelocque, Amiens Cedex 80039, France
E-mail: alejandro.franco@u-picardie.fr

The ORCID identification number(s) for the author(s) of this article can be found under https://doi.org/10.1002/smll.202107720.

J. Yu, G. Shukla, O. Arcelus, A. Shodiev, A. A. Franco
Réseau sur le Stockage Electrochimique de l'Energie (RS2E)
FR CNRS 3459
Hub de l'Energie
15 rue Baudelocque, Amiens Cedex 80039, France

R. P. Fornari, P. de Silva
Department of Energy Conversion and Storage
Technical University of Denmark
Anker Engelunds Vej, Building 301, Kongens Lyngby 2800, Denmark

A. A. Franco
ALISTORE-European Research Institute
FR CNRS 3104
Hub de l'Energie
15 rue Baudelocque, Amiens Cedex 80039, France

A. A. Franco
Institut Universitaire de France
103 Boulevard Saint Michel, Paris 75005, France

production cost.[7] ORFBs can overcome the drawbacks of several metal-based RFBs in the context of environmental sustainability.[8] Furthermore, even if the long-term performance of ORFBs is not yet as good as VRFBs, their capital cost is still competitive in the long term.[8,9]

In the past decades, many promising organic molecules have been reported as redox-active material candidates for ORFBs, such as anthraquinone-based compounds,[10–15] alkoxybenzene-based compounds,[16–18] and 2,2,6,6-tetramethyl-piperidin-1-oxyl.[19–24] Recently, Liu et al. developed a low-cost aqueous ORFB using methyl viologen (MV, anolyte) and 4-hydroxy-2,2,6,6-tetramethylpiperidin-1-oxyl (4-HO-TEMPO, catholyte) with a NaCl-based supporting electrolyte.[19] This newly reported redox couple demonstrates strong advantages, such as long-term cycling, low-cost raw materials, and an eco-friendly aqueous electrolyte. The cell reaction can be described as follows

$$MV^+ + [4-HO-TEMPO]^+ \xrightarrow{\text{Discharge}} MV^{2+} + 4-HO-TEMPO \quad (1)$$
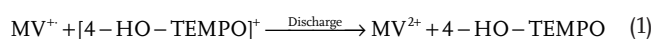
The electrochemical performance of the underlying reaction mechanisms is heavily influenced by numerous side reactions and interactions, including adsorption and desorption between the active material and the electrode, wherein the electrode consists of carbon felt or carbon foam.[22,25–27] Thus, for the development of this technology, a deeper understanding of interfacial dynamics at the electrode–electrolyte interfaces of this complex system is crucial and highly reliant on computational simulations.

Most modeling studies on RFBs have reported computational approaches of metal-based redox couples,[28–34] yet very few reports study of redox-active organic molecules. At the molecular level, density functional theory (DFT) has been widely applied in screening redox couples due to the reasonable computational cost and adequate accuracy.[35,36] Ding and Yu reported a comparison of electrochemical characteristics between a series of quinone compounds via DFT calculations combined with experiments.[37] At the mesoscale level, Li developed a 3D model of a metal-free quinone-based organic–inorganic RFB to investigate the impact of electrode thickness on cell performance.[38] Zhang et al. developed a 3D Lattice Boltzmann method model to study the role of the porous electrode microstructure in redox flow battery performance.[39] Nonetheless, the interactions between different phases and their impact on electrochemical kinetics are rarely discussed.

Numerous physical and chemical processes occur at the electrode/electrolyte interface, including adsorption/desorption, electron transfer, chemical reaction, and mass transfer, which can be characterized as stochastic and complex, and cannot be directly linked to macroscale observables. To address this kind of problem, many researchers have adopted the kinetic Monte Carlo (kMC) computational approaches.[40–42] As a branch of the Monte Carlo method, kMC aims to tackle the dynamic properties of a system in addition to equilibrium characteristics, to solve complex problems using random numbers.[43] It has been well applied to computational chemistry and materials science during the past few decades due to its outstanding efficiency, simplicity, and versatility. For instance, Modak and Lust developed a kMC model to simulate the ion concentration profiles

and the electric double layer (EDL) structure of a doped electrode for a solid-oxide fuel cell, which were found to be identical to the predictions of the analytical model.[44] Methekar et al. applied kMC to investigate the heterogeneity of the passive solid-electrolyte-interface formation in a graphite anode.[41]

To further investigate the electrode kinetics of organic redox flow batteries, this study reports a novel kMC model combined with the DFT and EDL approach to further investigate the electrochemical behavior at the electrode-anolyte interface of an MV-based aqueous ORFB system (**Figure 1**).

2. Model Description

The in house kMC model that we developed in this study implements the so-called variable step size method (VSSM), one of the most frequently applied kMC methods.[45,46] The VSSM model is coupled with an EDL approach to explicitly solve the electrical field distribution inside the EDL region. The logic flow of the in-house VSSM model is listed as follows (**Figure 2**):

1. The VSSM model is coupled with an EDL approach to explicitly solve the electrical field distribution inside the EDL region. The logic flow of our in house VSSM model is as follows (Figure 2);
2. Define an initial state of the system and input conditions (anolyte concentration, input current densities...);
3. Search for all the possible events for the current state and calculate the rate, k_i, of each event i;
4. Generate the first random number, ρ_1, to choose a possible event;
5. Generate the second random number, ρ_2, and update the simulation clock by adding a time step, Δt;
6. Execute the chosen event, update the system configuration accordingly and calculate the electrode charge density, σ;
7. Solve the EDL model to obtain the electric field distribution inside the EDL region;
8. Check if the system meets the cut-off condition or not. If not, pass to step 8). If so, terminate the simulation;
9. Update the kinetics for different events and restart the kMC algorithm with the new kinetics.

2.1. General Assumptions and Model Setup

In this study, the kMC model has been developed with an "on-lattice" approach for the electrode/anolyte system under the following assumptions: i) the system is simulated under isothermal conditions, and temperature fluctuations are not taken into consideration, ii) the electrode surface of the redox flow battery system is considered flat at the simulation scale, iii) the cross-over of redox-active molecules and ions at the membrane is not considered, iv) the catholyte side is assumed to be 4-HO-TEMPO, reacting symmetrically, as the anolyte side, and v) the thickness of the EDL region is considered to be much lower than that of the hydrodynamic boundary layer. Our target process is the discharge of MV+ anolyte. Additionally, the motion of the molecule and the disproportionation of $(MV_2)^{2+}$ are considered explicitly on the 3D lattice.
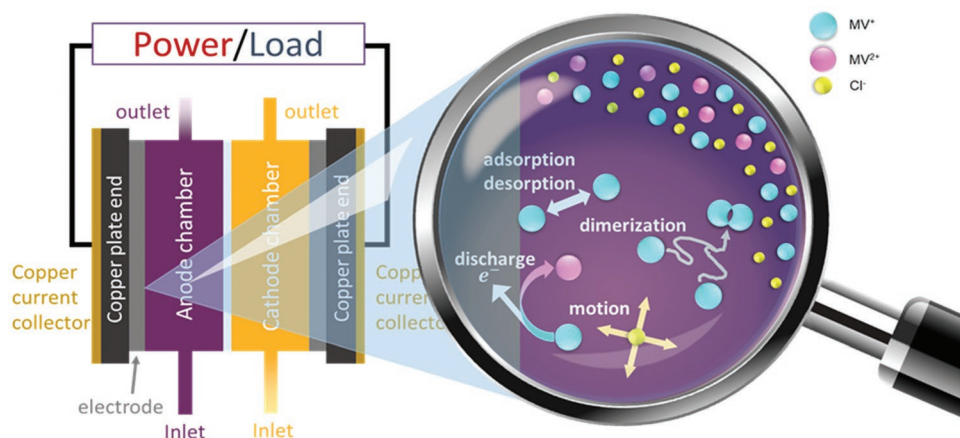
Figure 1. The interface between the anolyte and electrode targeted in this modeling study.

Furthermore, the unit grid size of the kMC model consists of cubic meshes of edge length 8 Å, which has been selected to mimic the size of the solvated methyl viologen molecule. The solvated MV^+, MV^{2+}, MV^0, and Cl^- are represented as hard spherical entities on the simulation grid, and their specific conformations have been neglected. The size difference between methyl viologen species and chloride ions is not considered in the mesh since the total number of grid unit cells is large enough to achieve the target concentration. However, the respective sizes of the molecules and ions are taken into consideration when performing calculations. The solvent is represented as a continuum and not in an explicit manner. The impact of solvent on the ionic motion of the charged species is captured by considering the Frumkin effect, as discussed in the Supporting Information S1.

The anolyte flow is assumed to be continuously renewed along the z-axis direction during operation, and the back-flow is neglected. In the z-axis direction, the simulation box is separated into two sections, the compact layer and the diffuse layer, regarding the EDL structure. Due to the grid size limitation, the Inner Helmholtz layer and the Outer Helmholtz layer are not differentiated in the compact layer whose thickness is set to 8 Å, i.e., one grid unit size, and the rest of the simulation box represents the diffuse layer. The electrode surface is located on the top of the simulation box, as shown in **Figure 3**.

The length of the simulation box is set to be the Debye length calculated through Equation (2)

$$L_D = \sqrt{\frac{\varepsilon_0 \varepsilon_{DL} k_B T}{\sum_i^i c_0^i (z_i e)^2}}$$ (2)

Where, ε_0 and ε_{DL} are the permittivity of vacuum and the relative permittivity of the anolyte, respectively. k_B is the Boltzmann constant, and T is the absolute temperature. c_0^i and z_i are the concentration and the valence, respectively, of the ionic species i, and e is the elementary charge.

The mass transport within the bulk solution is only driven by diffusion, since the length of the simulation box covers the EDL, which is assumed to be the boundary for migration.

Additionally, the convection flux has been ignored because the scale of the model is smaller than the boundary layer thickness of fluid dynamics (the latter estimated to be in the micrometric scale).[47] We assume the bottom layer to be the transition between the EDL region and the bulk anolyte, where the concentrations of each species are maintained as the bulk value and the charge neutrality is ensured, while the electrical field also drives the ionic motion. Unlike a macroscopic solution system, neutrality and mass conservation inside the EDL region are no longer respected.[48] Periodic boundary conditions are applied at the lateral borders (x-axis and y-axis).

2.2. EDL Approach

To include the electrochemical behavior in the simulation, we implemented an EDL approach in our kMC model, which is solved at each iteration of the kMC algorithm. The classic Gouy–Chapman–Stern theory was adapted in our EDL model,[49] which consists of a compact layer filled by solvent molecules and ions, which may or may not be adsorbed, and a diffuse layer where the concentration of the oppositely charged ions decreases along with the distance from the surface. The geometrical structure of the EDL is shown in **Figure 4**.

The electrostatic potential of the rigid electrode surface, φ, is calculated by the sum of the electrostatic potential outside the compact layer, Φ_L, i.e., the potential at the interface between the compact layer and the diffuse layer, and the potential drop, η, between the electrode and the anolyte (Equation (3))[50]

$$\varphi = \phi_L + \eta$$ (3)

2.2.1. Compact Layer Model

To calculate the potential drop through the compact layer, η, we consider it as the sum of two different potential drops, $\Delta\eta_1$ and $\Delta\eta_2$. $\Delta\eta_1$ is the potential drop related to the compact layer's thickness and the charge density on the electrode surface σ.
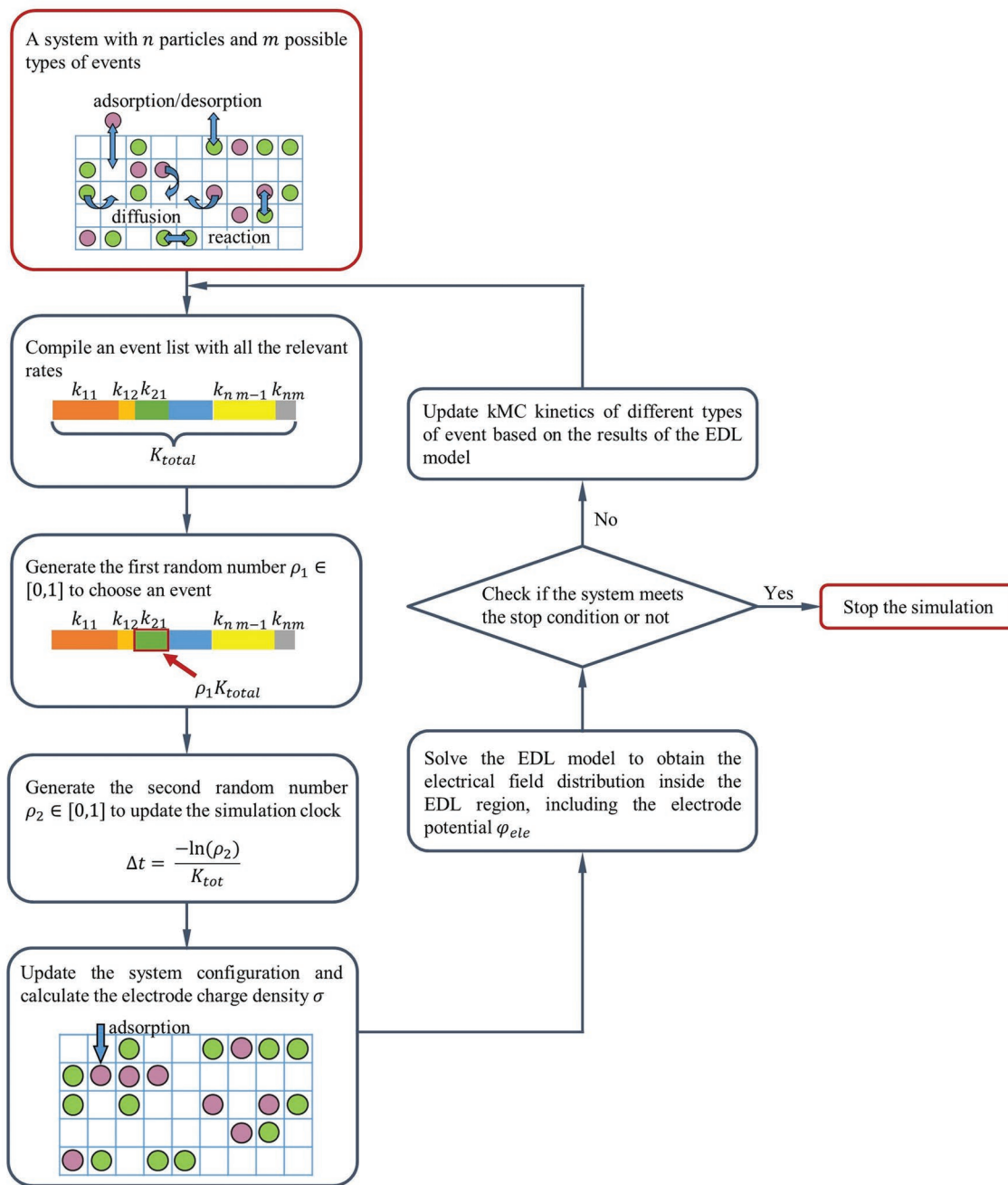
**ADVANCED
SCIENCE NEWS**

www.advancedsciencenews.com

**NANO · MICRO
small**

www.small-journal.com

Figure 2. Computational workflow behind our kMC – VSSM algorithm.

$\Delta \eta_2$ is the potential drop related to the adsorbed species charge density, Γ, which is also a function of σ.

The charge density on the electrode surface, σ, is the accumulated charge during the electrochemical process, expressed through the input current density, J_{inp} and the Faradaic current density, J_{Far}, as shown in Equation (4)

$$J_{inp} - J_{Far} = -\frac{\partial \sigma}{\partial t} \tag{4}$$

J_{Far} is generated by the oxidation reaction on the electrode surface and calculated through Equation (5), where ΔQ is the total charge transferred by all the electrochemical reaction events, S is the electrode surface, and Δt is the total simulation time

$$J_{Far} = \frac{\Delta Q}{S \Delta t} \tag{5}$$

The value of charge density on the electrode surface, σ, impacts both potential drops, $\Delta \eta_1$ and $\Delta \eta_2$, which then affect
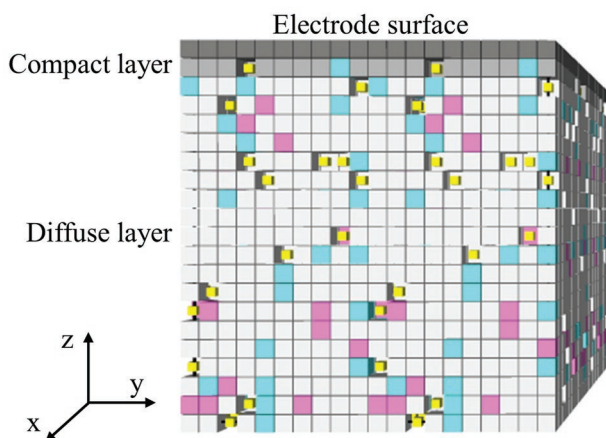
Figure 3. 3D visualization of the simulation box and the initial configuration of the molecules and ions. The pink, blue, and yellow pixels represent the grid units occupied by MV^{2+}, MV^{+}, and Cl^{-}, respectively.

the discharging kinetics as a parameter for the kinetic event rates. The first potential drop, $\Delta\eta_1$, is expressed through Equation (6), where ε_{CL} is the relative electric permittivity of the compact layer

$$\Delta\eta_1 = \frac{\sigma d}{\varepsilon_0 \varepsilon_{CL}} \tag{6}$$

The second potential drop, $\Delta\eta_2$, considers both the adsorbed water dipoles and the charge density of the adsorbed MV ion. Thus, $\Delta\eta_2$ can be expressed as Equation (7)

$$\Delta\eta_2 = \frac{\Gamma(\sigma)}{\varepsilon_0 \varepsilon_{DL}} \tag{7}$$
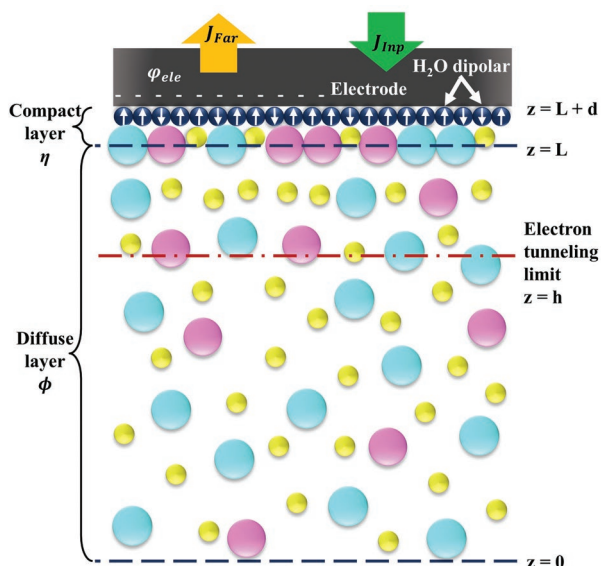

Figure 4. Schematic illustration of the EDL structure accounted for in our model. The thickness of the diffuse layer is L. The thickness of the compact layer is d. Oriented water dipoles are indicated with arrows.

where ε_{DL} is the relative electric permittivity of the diffuse layer. For the detailed calculation of the adsorbed species charge density, $\Gamma(\sigma)$, please refer to the Supporting information S1.

By substituting the values of $\Delta\eta_1$ and $\Delta\eta_2$, we obtain the total potential drop through the compact layer, η, which impacts the electrochemical kinetics through the $f(\sigma)$ term (Equation (8))

$$f(\sigma) = \alpha F\eta = \alpha F\left(\frac{\sigma d}{\varepsilon_0 \varepsilon_{CL}} + \frac{\Gamma(\sigma)}{\varepsilon_0 \varepsilon_{DL}}\right) \tag{8}$$

α is a prefactor representing the reaction's equilibrium state, F is the Faraday constant, and $f(\sigma)$ is an additional term incorporating the effective reorganization energy calculation, which is explained later in Equation (16).

2.2.2. Diffuse Layer Model

The calculation of the electric potential, ϕ, and the electric field, E, within the diffuse layer was carried out by integrating a solver for the Poisson equation within the kMC simulation. The Poisson equation is defined as

$$\nabla^2 \phi = -\frac{\rho}{\varepsilon_0 \varepsilon_{DL}} \tag{9}$$

where ρ is the volume charge density.

The differential equation (Equation (9)) is then solved using the finite difference method on a finer cubic grid with indices i, j, and k. It is composed of even subdivisions of the original kMC grid, such that the centers of particles in the original grid always lie on top of the grid points used for solving Equation (9). We approximate MV^{+}, MV^{2+}, and Cl^{-} as point charges, defining the volume charge density as follows

$$\rho(r) = \sum_{i=1}^{N} e z_i \delta(r - r_i) \tag{10}$$

where δ is the Dirac delta function.

The boundary conditions employed for solving the Poisson equation in a simulation box with dimensions L_x, L_y, and L_z are as follows

– Dirichlet boundary conditions: $\phi_{ij0} = 0$, simulating the reference potential at the bulk anolyte;
– Neumann boundary conditions: $\frac{\partial\phi}{\partial z}\Big|_{ijL_z} = \frac{\sigma}{\varepsilon_0 \varepsilon_{DL}}$;
– Periodic boundary conditions at $i = j = 0$: $i = Lx$, and $j = L_x$;

The discretization of Equation (10) leads to a system of linear equations, as shown below

$$\mathbb{A} \cdot x = b \tag{11}$$

where $\mathbb{A}$ is the coefficient matrix containing the linear relationship between the electric potential and the charge density, x is a flattened vector containing the electric potential values at grid points i, j, and k, and b contains the information of the charge density and the boundary conditions. A direct solution

ADVANCED
SCIENCE NEWS
www.advancedsciencenews.com

NANO · MICRO
small
www.small-journal.com

by inversion of matrix $\mathbb{A}$ is possible; however, it is essential to realize that, by construction, matrix $\mathbb{A}$ is sparse. We can then take full advantage of the SciPy[51] sparse solvers for an almost tenfold performance boost, which is critical, given that Equation (10) is going to be solved once per kMC iteration, and it is, therefore, essential to avoid significant bottlenecks.

By calculating the gradient of the electrical potential, ϕ, inside the diffuse layer, we obtain the following electrical field distribution at each grid node of the diffuse layer

$$E_{(i,j,k)} = -\nabla \phi_{(i,j,k)} \tag{12}$$

2.3. Basic Events and Events Rate Calculations in the kMC Model

2.3.1. Hopping Event and Hopping Rate

The event of molecular displacement considered in this work is generated only by translation with a step size equaling the mesh size, and no overlapping in the grid is tolerated. The driving forces for the hopping event are diffusion and migration. All the considered species are assumed to be mobile except MV^0, due to its insolubility.

The diffusion rate, K_{diff}, is measured

$$K_{\text{diff}} = \frac{D_{\text{diff}}}{A} \tag{13}$$

and the diffusion coefficient, D_{diff}, is expressed by the Stokes–Einstein equation as presented in Equation (14),

$$D_{\text{diff}} = \frac{k_B T}{6 \pi \mu r_i} \tag{14}$$

where μ is the dynamic viscosity of the anolyte, r_i is the hydrodynamic radius of the considered species i, and A is the cross-sectional surface area of the considered species.[52,53]

The Stokes–Einstein equation takes the dynamic viscosity of the anolyte and the size of the molecule into consideration. By substituting the corresponding values of $MV^{+\cdot}$ and MV^{2+}, diffusion coefficients of 5.05×10^{-6} cm^2 s^{-1} are obtained, which is within the range of the experimental values for low concentration methyl viologen anolytes.[54]

The electrical field generated by the EDL structure influences the displacement of the concerned particles by migration. To include this mechanism, we describe the migration and the diffusion together by considering the initial diffusion rate as the hopping rate and adding the Arrhenius-type expression of the impact of electrical field on the jumping frequency of the species, as shown in Equation (15)

$$K_{\text{hop}} = a K_{\text{diff}} \exp\left(\frac{\pm z_i e r_i E_{(x,y,z)}}{k_B T}\right) \tag{15}$$

The numerator of the exponential term is the work done by the electrical field to generate the hopping event. The value of the electrical field $E_{(x,y,z)}$ in Equation (15) corresponds to the

position of each displaceable particle position on the simulation grid. The "$\pm$" sign depends on the charge of the concerned particle, the hopping direction, and the electrical field direction. For instance, when considering a hopping event along the electrical field direction of a positively charged particle, the electrical field assists the hopping event and increases the hopping rate. Furthermore, a hopping event in the opposite direction is unfavorable under the same electrical field, which reduces the hopping rate. Here, a is a proportionality factor to modulate the impact of the electrical field on the ionic displacement.

2.3.2. Electrochemical Reaction Rate

This work aims to study the electrochemical kinetics of the methyl viologen system. Our target electrochemical reaction involves the oxidation of $MV^{+\cdot}$, which only occurs within the electronic tunneling distance, as shown in Figure 3. Eyring's expression from the transition-state theory describes the redox reaction kinetics through the activation energy E_a.

In our case, the electron transfer takes place in the solution. Thus, we consider the reorganization energy, E_λ, from Marcus–Hush theory,[55,56] which captures the free energy barrier of the electron transfer in the anolyte as the energy barrier for the electron transfer process. Furthermore, previous work by our group demonstrated that the value of E_λ needed to be corrected by adding the $f(\sigma)$ term (Equation (8)),[46,57,58] which is a function to consider the impact of the electrode surface charge density, σ, on the electrochemical reactions. After the correction, the electrochemical reaction rate is expressed as

$$K_{\text{dis}} = \kappa_0 \frac{k_B T}{h} \exp\left(\frac{-E_\lambda \mp f(\sigma)}{RT}\right) \tag{16}$$

where κ_0 stands for the vibrational frequency of the transition state, h and R are the Planck constant and the ideal gas constant, respectively, and $-E_\lambda \mp f(\sigma)$ is the effective reorganization energy, where the sign depends on whether the occurring reaction is oxidation or reduction.

The reorganization energy, E_λ, it is usually partitioned into inner-sphere and outer-sphere components, such that $E_\lambda = \lambda_o + \lambda_i$. The outer-sphere reorganization energy, λ_o, accounts for the change in polarization of the solvent molecules, which has little dependence on the molecular shape and internal degrees of freedom.[59] Hence, it can be assumed to be independent of the specific geometry of the species undergoing the electrochemical reaction,[60] and can be approximated by

$$\lambda_o = \frac{q}{8\pi} \left(\frac{1}{\varepsilon_{\text{opt}}} - \frac{1}{\varepsilon_{\text{st}}}\right)\left(\frac{1}{r_i} - \frac{1}{2d}\right) \tag{17}$$

Where d represents the electron tunneling distance, considered as the distance between the species and the electrode in the model. ε_{opt} and ε_{st} are, respectively, the optical and the static dielectric constant of the anolyte solution, where the latter is assumed to be the same value as the dielectric constant of the bulk solution.[59]

The inner-sphere or internal component, λ_i, reflects the energy relaxation associated with the changes in the internal

**ADVANCED
SCIENCE NEWS**

www.advancedsciencenews.com

**NANO · MICRO
small**

www.small-journal.com

molecular geometry that accompany the electron transfer, which is the main chemistry-specific parameter entering the reaction rate expression. λ_i is calculated using DFT, with the conventional four-point approach, as the average of the reorganization energies of the reactant (R) and product (P)

$$\lambda_i = \frac{1}{2}(\lambda_R + \lambda_P) = \frac{1}{2}[E(R,P) - E(R,R) + E(P,R) - E(P,P)] \quad (18)$$

where $E(R,R)$ and $E(P,P)$ are the geometry-optimized energies of the two species and the other two are single-point energies at the geometry of the other species. All energies were calculated with Q-Chem 5.2[61] at the B3LYP-D3BJ/6-31+G** level of theory with the conductor-like polarizable continuum model (C-PCM) implicit solvation model[62] using the relative permittivity of water ($\varepsilon_{\text{H}_2\text{O}} = 78.39$).

The four energies used for obtaining $\lambda_i = 0.263$ eV for the redox reaction $MV^{+\cdot} \rightleftarrows MV^{2+} + e^-$ are represented by the black dots in **Figure 5**, where the optimized geometries of the two species are also shown.

By combining the results from Equations (17) and (18), we obtained the total reorganization energies based on the electron tunneling distance, presented in **Figure 6**. As the electron tunneling distance expands, the reorganization energy increases rapidly and stabilizes after 3 nm. Thus, the electron tunneling limit is set at 3.2 nm in our model, which is the length of four lattice units.

2.3.3. Dimerization Event and Disproportionation Rate

According to Hu et al.,[22] the capacity loss of the MV-based anolyte is believed to be mainly caused by dimerization fol-
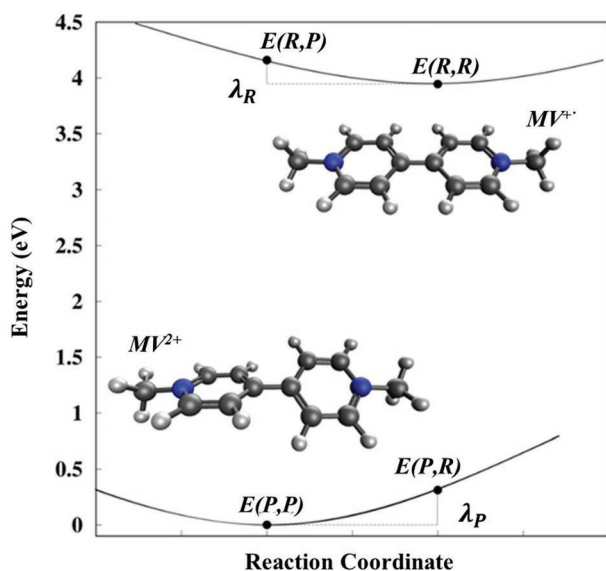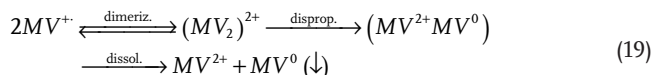

Figure 5. Illustration of the reorganization energy calculation along the reaction coordinate of the redox process $MV^{+\cdot} \rightleftarrows MV^{2+} + e^-$. The black dots are the energies of the two redox forms of methyl viologen, $MV^{+\cdot}$ and MV^{2+}, at their optimized geometries and at the geometry of the other form (all energies are relative to $E(P,P)$). The parabolae are just for illustration purposes and are not the computed potential energy surfaces.

lowed by disproportionation. In general, the formation of dimers and some trimers has been observed in low concentration anolytes (0.1 M). At high concentrations, 1 M or higher, it is reasonable to expect the formation of polymers.[64] These aggregation processes are generally reversible, but when two $MV^{+\cdot}$ radicals dimerize, the following disproportionation reaction can occur

$$2MV^{+\cdot} \xrightleftharpoons{\text{dimeriz.}} (MV_2)^{2+} \xrightarrow{\text{disprop.}} (MV^{2+}MV^0) \\ \xrightarrow{\text{dissol.}} MV^{2+} + MV^0 (\downarrow) \quad (19)$$

The main product of dimerization is the singlet dimer, $(MV_2)^{2+}$, where the unpaired electrons of two $MV^{+\cdot}$ are paired.[65] In the second reaction, one electron is transferred between the two molecules, generating a charge-separated dimer that subsequently dissociates into MV^{2+} and MV^0, where the latter is insoluble and precipitates out, causing capacity degradation.[26] Even though the thermodynamics favors the dimer's dissolution forming two $MV^{+\cdot}$ rather than the disproportionation,[66] the precipitation of MV^0 shifts the reaction to the right and causes capacity loss over long time scales. Since the disproportionation event has a much slower kinetics compared to the dimerization process, it is the dominant event in the degradation process.

Disproportionation is also included in our model to simulate the degradation of the target ORFB system. A degradation event is said to occur only when two $MV^{+\cdot}$ are located in neighboring grid units. If the disproportionation event is chosen, the dimer is assumed to decompose immediately and form MV^{2+} and MV^0. The degradation kinetics is described by a rate constant, K_{dispr} (Equation (20)), calculated by the Eyring equation

$$K_{\text{dispr}} = \kappa_0 \frac{k_B T}{h} \exp\left(\frac{-\lambda_i^{\text{dispr.}}}{RT}\right) \quad (20)$$

The parameter determining the disproportionation kinetics is the internal reorganization energy, $\lambda_i^{\text{dispr.}} = 0.640$ eV of the reaction $(MV_2)^{2+} \xrightarrow{\text{disprop.}} (MV^{2+} + MV^0)$, which was computed with the four-point approach using Equation (18). Both the reactant and product dimers were optimized with Q-Chem 5.2[61] at the B3LYP-D3BJ/6-31+G** level of theory with C-PCM in water.[62] The two energies of the charge-separated product dimer were computed with the constrained DFT method where the charge +2 is enforced on one of the molecules.[67] The energies and optimized structures of the reactant and product dimers are shown in **Figure 7**.

2.4. Computational Details

The in-house kMC model was fully coded in the Python 3 programming language. All the simulations were carried out in an eight-core Intel i7 workstation. The calculation time depends on the concentration in the target system, which varies from 5 days to a week. Further details of the parameter values are provided in the Supporting Information S2.

The model was tested under galvanostatic conditions with different anolyte concentrations and input current densities. At
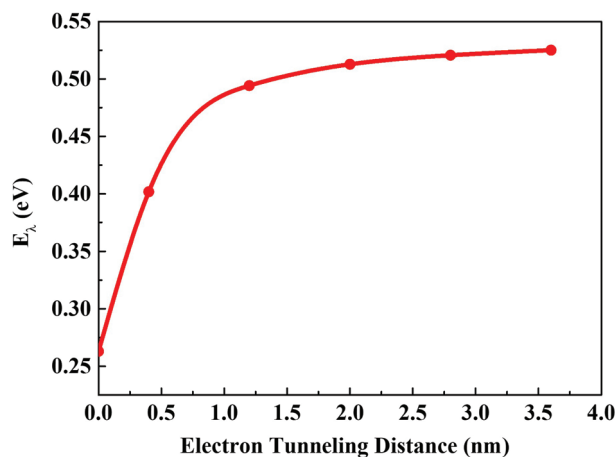
ADVANCED
SCIENCE NEWS
www.advancedsciencenews.com

NANO · MICRO
small
www.small-journal.com

Figure 6. Reorganization energy, E_λ, calculated with the sum of Equations (17) and (18) for six data points, using $\varepsilon_{st} = 72\varepsilon_0$ for the bulk anolyte permittivity,[63] and $\varepsilon_{opt} = 6.2\varepsilon_0$ for the compact layer permittivity.[57]

the initial phase, the system is assumed to be in a steady state where the electrode potential equals the standard electrode potential of MV (–0.45 V vs SHE), and all the ions are randomly arranged in the grid. Then, the simulation is launched with the initial electrode potential and an imposed current density, J_{inp} (cf. Figure 3).

3. Results and Discussions

The model was first tested under the anolyte concentrations of 1.0 M, with a constant input current density of
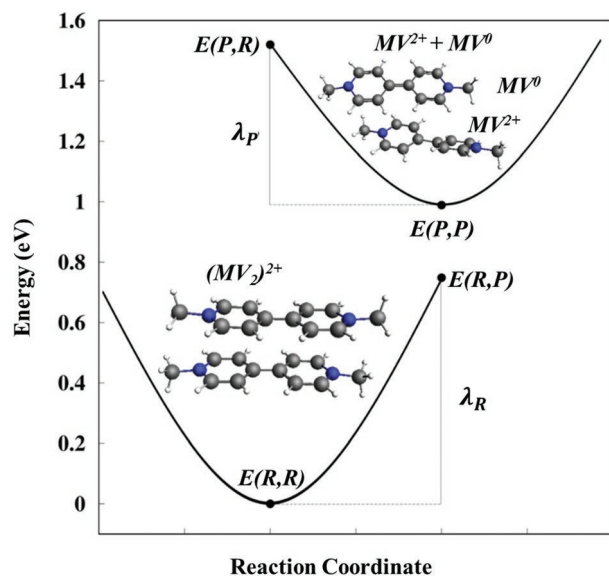

Figure 7. Illustration of the reorganization energy calculation along the reaction coordinate of the disproportionation process $(MV_2)^{2+} \rightarrow MV^{2+}+MV^0$. The black dots are the energies of the two dimers $(MV_2)^{2+}$ and $(MV^{2+} + MV^0)$ at their optimized geometries and the geometry of the other form (all energies are relative to E(R,R)). The parabolae are just for illustration purposes and are not the computed potential energy surfaces.

$J_{inp} = 50$ mA cm^{-2}. The results of the galvanostatic simulations are presented in **Figure 8**. The corresponding discharge video is available in the Supporting Information. In the first few nanoseconds of discharge, which is hereafter referred to as the activation state of discharge, the system is dominated by electrochemical reactions due to the significant reaction rate and all the $MV^{+\cdot}$ available within the tunneling distance accessible for discharge. Along with the electrochemical reaction events, electrons transfer from the active material, $MV^{+\cdot}$, to the electrode, and negative charges start to accumulate on the electrode surface, leading to an acute increase in the electrode potential, and a drop in the electrode charge density, as shown in Figure 8a,c.

The accumulated negative charge also negatively impacts the electron transfer rate, as indicated in Equations (6), (7), and (16). Furthermore, as the discharge continues, the accumulated negative charges on the electrode attract positively charged species. Due to the electrosorption, less accessible grid units are left inside the tunneling distance. The limited number of available sites takes the volume limitation into account. For $MV^{+\cdot}$ present outside the tunneling distance, no electrochemical reaction occurs until they reach the electrode. Due to these two reasons, the discharging process slows down, leading to a steady-state system dominated by ionic displacement, where the displaceable species, $MV^{+\cdot}$, MV^{2+}, and Cl^-, start to redistribute in the electrical double layer range under the impact of the electrostatic field generated by the electrochemical reaction.

Figure 8b demonstrates the concentration evolution of each species during the discharging process. The concentration of $MV^{+\cdot}$, MV^{2+}, and Cl^- reach a steady level after the activation state of the model. However, in the considered degradation event, the precipitation of MV^0 is insignificant; the relatively high organization energy leads to a low disproportionation rate. While the difference in the organization energy between the electron transfer event and the disproportionation event is less than 0.4 eV, the resulting kinetic rate difference is in the magnitude of 10^7. From Equations (16) and (20), we obtained an electron transfer rate of $K_{dis} = 1.44 \times 10^9$ s^{-1} at the beginning of discharge and a disproportionation rate of $K_{dispr} = 93$ s^{-1}. Thus, the disproportionation event is almost neglected in the compiled rate list of the kMC algorithm. Therefore, even though the dimerization followed by disproportionation is the generally acknowledged degradation mechanism for viologen compounds, the slow kinetics of disproportionation estimated from DFT suggests capacity fade over longer time scales than the ones addressed by our model.

The increasing value of the electrode charge density during the discharge process was also found to influence the EDL structure. **Figure 9**a–d shows the negative and positive charge density profiles along the z-axis during the discharge process, which are obtained from the post analysis of the simulation grid. The positive curve (red) considers the charge density at each layer provided by $MV^{+\cdot}$ and MV^{2+}, while the negative curve (black) considers only the charge density at each layer provided by the Cl^-. The blue shaded area on the x-axis is the net charge density profile, obtained from the sum of the positive and negative charges. The video of charge density profile evolution during the discharge process is also provided in the Supporting Information.
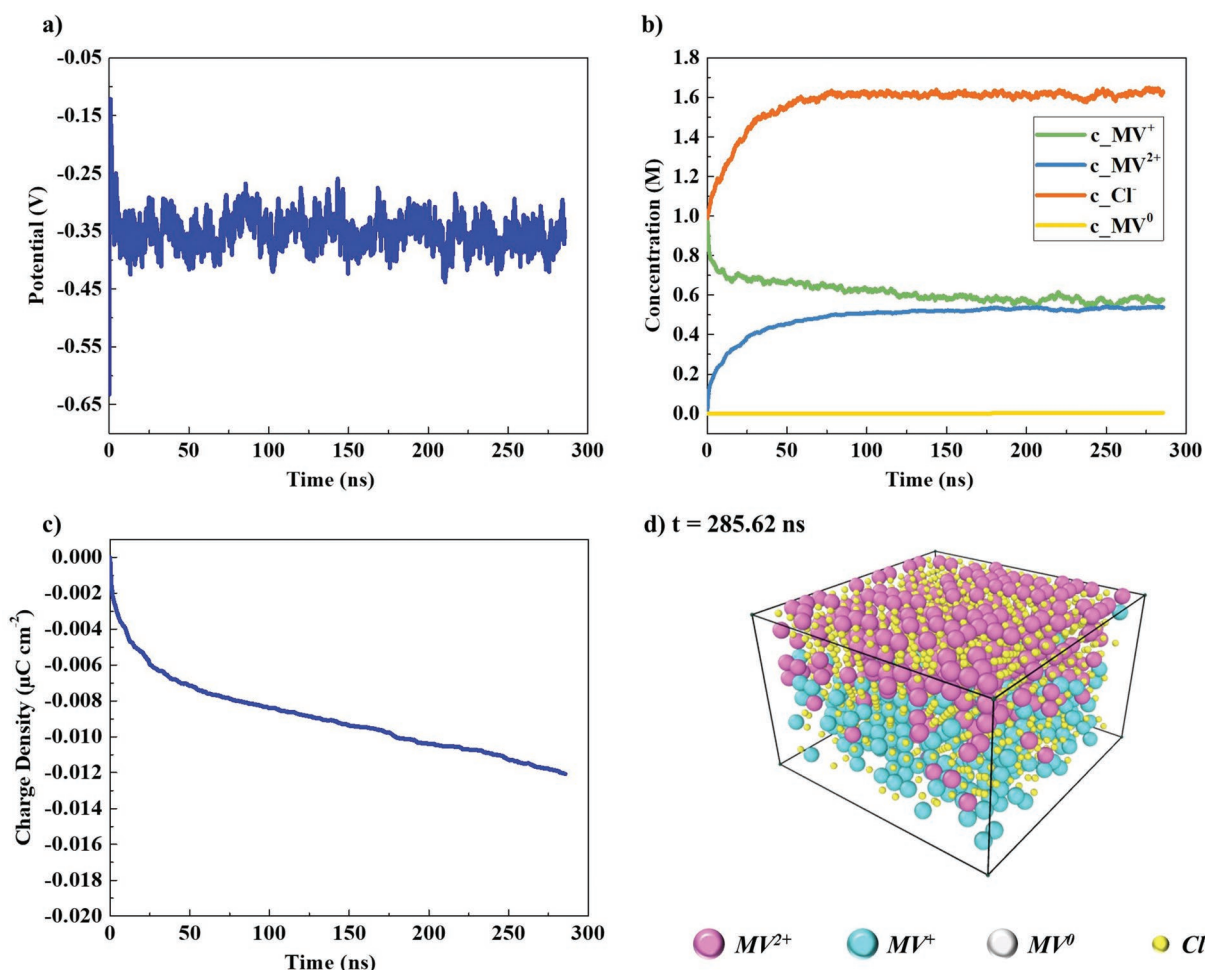
ADVANCED
SCIENCE NEWS
www.advancedsciencenews.com

NANO · MICRO
small
www.small-journal.com

Figure 8. Galvanostatic discharge simulations with an MV concentration of 1.0 M and input current density J_{inp} = 50 mA cm^{-2}. a) electrode potential; b) concentration of different species; c) electrode charge density; d) illustration of the entire simulation box without the electrode on the top at the steady-state with t = 285.62 ns.

Unlike the classic continuum Gouy–Chapman model, where the charge density profile decreases continuously and sharply, an intense charge oscillation between the positively and negatively charged ions is observed (Figure 9b), which was also reported in Molecular Dynamics (MD) simulations.[68] This oscillation is due to the explicit description of charged ions in the lattice. When the discharge starts, many MV^{2+} are produced from electron transfer. The opposite charge accumulated on the electrode attracts the MV^{2+}; thus, it stays close to the electrode surface and forms a compact layer. As the discharge proceeds, the electrical field becomes more intense and homogeneously distributed across the EDL section, forming the entire EDL structure. The intensity of the charge density profile decreases progressively till the end of the EDL, i.e., the simulation box, as shown in Figure 9d. Unlike the MD simulation, where molecules and ions motion have no voxel limitations, the charge density profile obtained from this study oscillates regularly based on the grid unit size. Due to the volume limitation of the simulation box, the number of chemical species is limited; thus, the compact layer does not demonstrate the typical high charge density profile.

The model was then used to study the discharge behavior at five different anolyte concentrations (0.1 M, 0.25 M, 0.5 M, 0.75 M, and 1.0 M) with the same input current densities (50 mA cm^{-2}). The evolution of the electrode charge density and potential under different concentrations are shown in **Figure 10**a,b, respectively. When the active material concentration decreases, the amount of $MV^{+\cdot}$ that discharges within the tunneling distance decreases, leading to a milder increase in potential at the activation stage. On the other side, the available sites near the electrode surface can more easily be saturated by the active species, allowing the system to reach the steady state faster.

Regarding the EDL structure at the steady state, the charge density in the compact layer is limited by the volume limitation, while the charge density at the boundary between the EDL and the bulk anolyte is limited by the input anolyte concentration. As the concentration decreases, the EDL thickness (simulation box) increases, as expressed in Equation (2). Thus, the EDL structure becomes less compact due to the concentration difference between the electrode surface and the bulk anolyte. The charge density profiles at the steady-state of the simulation
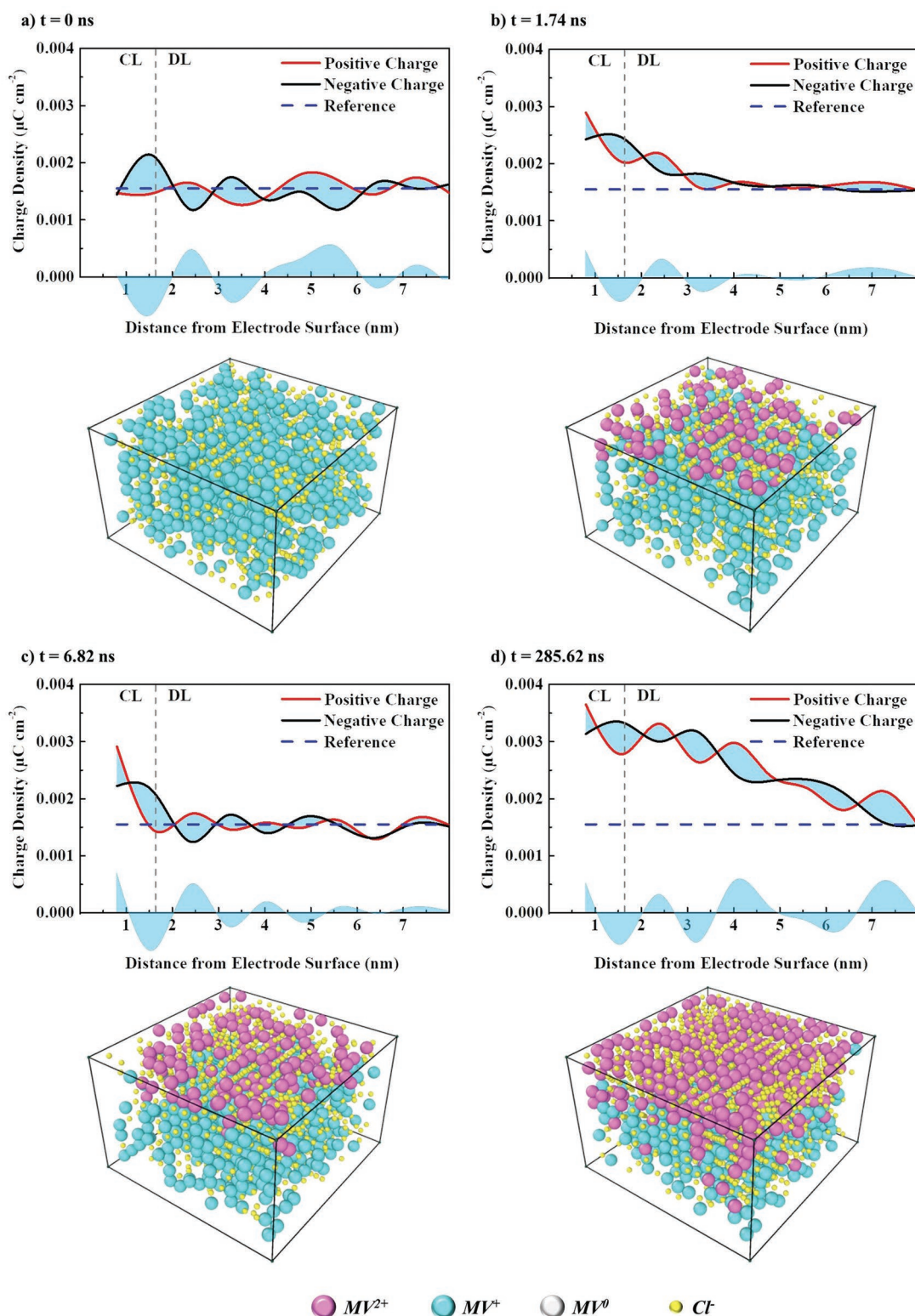
ADVANCED
SCIENCE NEWS
www.advancedsciencenews.com

NANO · MICRO
small
www.small-journal.com

Figure 9. Calculated charge density profiles in the simulation grid during the discharge process. The red and black lines represent the positive charge density and the absolute value of the negative charge density at each layer, respectively. The blue dashed line represents the absolute charge density of positive/negative species in the bulk anolyte. The thickness range of the compact and diffuse layers are also indicated.

with different anolyte concentrations are provided in Figure S1 of the Supporting Information.

The impact of different input current densities was also studied with our model. We expanded our simulation conditions
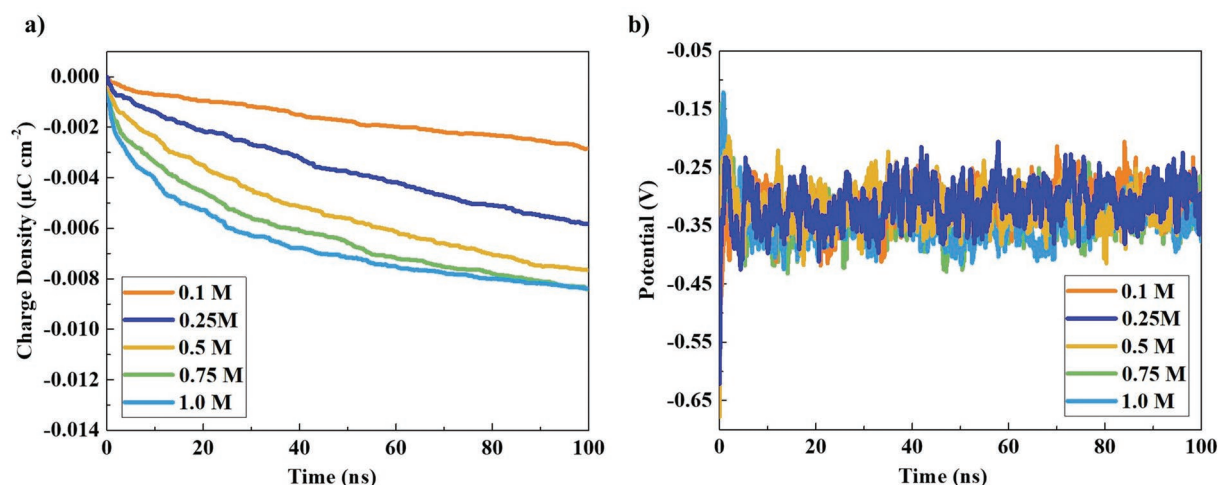
ADVANCED
SCIENCE NEWS
www.advancedsciencenews.com

NANO · MICRO
small
www.small-journal.com

Figure 10. Simulated electrode charge density and potentials for 5 different anolyte concentrations: 0.1 ᴍ, 0.25 ᴍ, 0.5 ᴍ, 0.75 ᴍ, and 1.0 ᴍ, and 1.0 ᴍ. The input current density was set at 50 mA cm⁻².

to a combination of five anolyte concentrations (0.1 ᴍ, 0.25 ᴍ, 0.5 ᴍ, 0.75 ᴍ, and 1.0 ᴍ) and four input current densities (50, 100, 150, 200 mA cm⁻²). The final steady-state potential was extracted and plotted in **Figure 11**. Due to the stochasticity of ion displacement, the potential was seen to fluctuate around a certain value. Thus, we took the average value of the potential after the system entered the steady state. As calculated in Equation (4), the increase of input current density leads to the increase in the absolute value of the charge density, which reduces the final steady-state electrode potential (Equation (9)). As shown in the chart, a higher concentration leads to a lower steady-state potential, which is in agreement with the Nernst equation. On the contrary, the model is not sensitive enough in terms of the input current density, which can be attributed to the neglected electrolyte resistance.

4. Conclusion

In this work, we presented our novel kMC model with a molecular-scale resolution of the galvanostatic discharging process of a methyl viologen anode system to study the underlying interfacial dynamics with a molecular-scale resolution. The kMC algorithm tackles the interfacial electrochemical kinetics with input parameters obtained from DFT calculations, while the EDL model simulates the electrostatic impact on the discharging behavior.

Our model simulates three electrode processes: ionic motion, electrochemical reaction, and degradation. The ionic motion event rate is calculated dynamically by considering the impact of electric field distribution. The electrochemical reaction rate is calculated through the Eyring equation and the effective
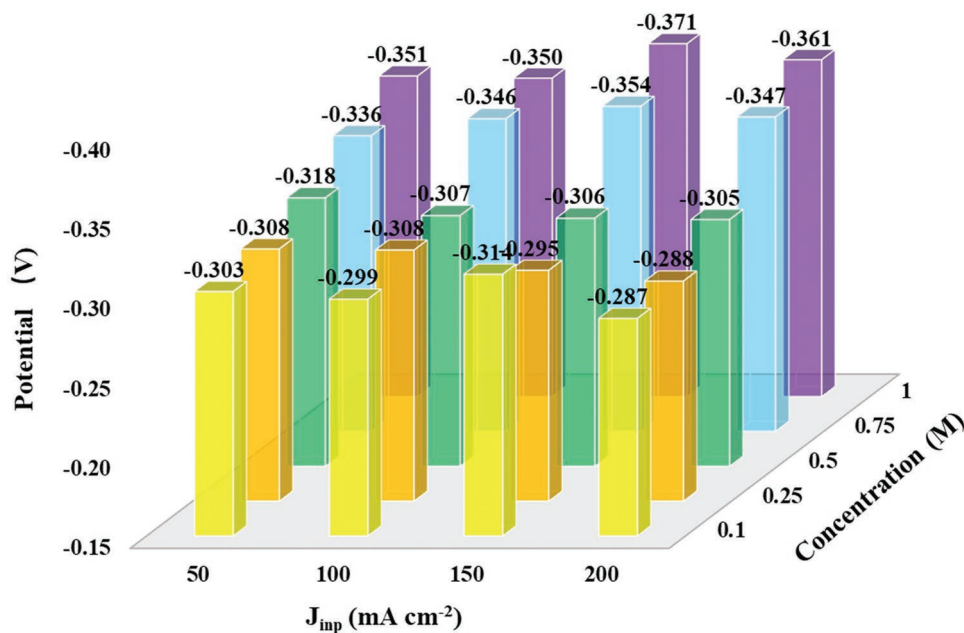

Figure 11. Simulated electrode potential at steady-state under different combinations of anolyte concentration and input current densities.

ADVANCED
SCIENCE NEWS
www.advancedsciencenews.com

NANO · MICRO
small
www.small-journal.com

reorganization energy, where the latter is obtained from DFT calculations and the potential drop through the compact layer. The degradation event consists of the disproportionation of a formed dimer in which the precipitation causes capacity fade. Thus, the disproportionation rate is considered as the degradation rate.

The model was used to simulate galvanostatic discharge at different anolyte concentrations and input current densities. The EDL formation was captured through the simulations, which demonstrated a substantial impact on ionic transport and electrode kinetics. Furthermore, the obtained EDL structure of charge inversion was found to correspond to the results reported in literature for other systems based on the Molecular Dynamics approach. The potential evolution presents different events dominating the system during the discharge process, where the electrochemical reaction is observed more at the beginning of discharge, and the hopping event is more common in the steady-state. The calculated concentration of different species demonstrates that the disproportionation of $(MV_2)^{2+}$ is the reason for long-term capacity fade, which is not likely to be captured within the nanosecond range of these kMC simulations. On the contrary, it is noticed that positively charged species ($MV^{+\cdot}$ and MV^{2+}) are trapped on the electrode surface due to the electrical field impact, which hinders the active material in the diffuse layer from approaching the electrode and reacting.

The model demonstrates that the interplay between the electrostatic impact and the electrochemical kinetics determines the final steady-state of the system, and the charge density at the electrode influences the system configuration, which determines the discharge rate and the electrode potential. The model's flexibility allows further applications of simulating the behavior of a target redox flow couple in an ORFB. With the help of DFT calculations, electrochemical kinetics can be obtained with simple experiments. The structure of this model also makes it possible to consider other events when needed.

In future studies, the adsorption/desorption events will be added to the model to investigate the interactions between active materials and the electrode surface thoroughly. Furthermore, a complete full cell kMC model with experimental validations is also under development. Therefore, the kMC model introduced in this paper paves the way toward the computational screening of active species by assessing their potential kinetics in electrochemical environments.

Supporting Information

Supporting Information is available from the Wiley Online Library or from the author.

Acknowledgements

Conflict of Interest

The authors declare no conflict of interest.

Data Availability Statement

The data that support the findings of this study are available from the corresponding author upon reasonable request.

Keywords

[1] K. Lourenssen, J. Williams, F. Ahmadpour, R. Clemmer, S. Tasnim, *J. Energy Storage* **2019**, *25*, 100844.

[2] P. Leung, A. A. Shah, L. Sanz, C. Flox, J. R. Morante, Q. Xu, M. R. Mohamed, C. Ponce de León, F. C. Walsh, *J. Power Sources* **2017**, *360*, 243.

[3] EASE/EERA, *European Energy Storage Technology Development Roadmap*, EASE, Brussels, Belgium **2017**, p. 128.

[4] M. Uhrig, S. Koenig, M. R. Suriyah, T. Leibfried, *Energy Procedia* **2016**, *99*, 35.

[5] A. Crawford, V. Viswanathan, D. Stephenson, W. Wang, E. Thomsen, D. Reed, B. Li, P. Balducci, M. Kintner-Meyer, V. Sprenkle, *J. Power Sources* **2015**, *293*, 388.

[6] A. Aihemaiti, J. Jiang, D. Li, T. Li, W. Zhang, X. Ding, *Environ. Sci. Pollut. Res.* **2017**, *24*, 26839.

[7] M. Van Dalen, J. O'Farrelly, *Johnson Matthey Technol. Rev.* **2018**, *62*, 185.

[8] J. Winsberg, T. Hagemann, T. Janoschka, M. D. Hager, U. S. Schubert, *Angew. Chem., – Int. Ed.* **2017**, *56*, 686.

[9] F. R. Brushett, M. J. Aziz, K. E. Rodby, *ACS Energy Lett.* **2020**, *5*, 879.

[10] B. Huskinson, M. P. Marshak, C. Suh, S. Er, M. R. Gerhardt, C. J. Galvin, X. Chen, A. Aspuru-Guzik, R. G. Gordon, M. J. Aziz, *Nature* **2014**, *505*, 195.

[11] M. R. Gerhardt, L. Tong, R. Gómez-Bombarelli, Q. Chen, M. P. Marshak, C. J. Galvin, A. Aspuru-Guzik, R. G. Gordon, M. J. Aziz, *Adv. Energy Mater.* **2017**, *7*, 1601488.

[12] B. Hu, J. Luo, M. Hu, B. Yuan, T. L. Liu, *Angew. Chem.* **2019**, *131*, 16782.

[13] B. Yang, A. Murali, A. Nirmalchandar, B. Jayathilake, G. K. S. Prakash, S. R. Narayanan, *J. Electrochem. Soc.* **2020**, *167*, 060520.

[14] A. W. Lantz, S. A. Shavalier, W. Schroeder, P. G. Rasmussen, *ACS Appl. Energy Mater.* **2019**, *2*, 7893.

[15] Y. Zhen, C. Zhang, J. Yuan, Y. Zhao, Y. Li, *J. Power Sources* **2020**, *480*, 229132.

[16] J. Huang, L. Su, J. A. Kowalski, J. L. Barton, M. Ferrandon, A. K. Burrell, F. R. Brushett, L. Zhang, *J. Mater. Chem. A* **2015**, *3*, 14971.

[17] F. R. Brushett, J. T. Vaughey, A. N. Jansen, *Adv. Energy Mater.* **2012**, *2*, 1390.

[18] L. Zhang, Z. Zhang, P. C. Redfern, L. A. Curtiss, K. Amine, *Energy Environ. Sci.* **2012**, *5*, 8204.

[19] T. Liu, X. Wei, Z. Nie, V. Sprenkle, W. Wang, *Adv. Energy Mater.* **2016**, *6*, 1501449.

ADVANCED
SCIENCE NEWS
www.advancedsciencenews.com

NANO · MICRO
small
www.small-journal.com

[20] X. Wei, W. Xu, M. Vijayakumar, L. Cosimbescu, T. Liu, V. Sprenkle, W. Wang, *Adv. Mater.* **2014**, *26*, 7649.

[21] J. D. Milshtein, J. L. Barton, R. M. Darling, F. R. Brushett, *J. Power Sources* **2016**, *327*, 151.

[22] B. Hu, Y. Tang, J. Luo, G. Grove, Y. Guo, T. L. Liu, *Chem. Commun.* **2018**, *54*, 6871.

[23] J. Winsberg, T. Janoschka, S. Morgenstern, T. Hagemann, S. Muench, G. Hauffman, J.-F. Gohy, M. D. Hager, U. S. Schubert, *Adv. Mater.* **2016**, *28*, 2238.

[24] J. Winsberg, C. Stolze, S. Muench, F. Liedl, M. D. Hager, U. S. Schubert, *ACS Energy Lett.* **2016**, *1*, 1368.

[25] E. S. Beh, D. De Porcellinis, R. L. Gracia, K. T. Xia, R. G. Gordon, M. J. Aziz, J. A. Paulson, *ACS Energy Lett.* **2017**, *2*, 639.

[26] M. Mohammad, L. Naz, A. Rauf, S. Rauf, *J. Chem. Soc. Pakistan* **2013**, *35*, 659.

[27] Y. Liu, Y. Li, P. Zuo, Q. Chen, G. Tang, P. Sun, Z. Yang, T. Xu, *ChemSusChem* **2020**, *13*, 2245.

[28] M. Gautam, Z. M. Bhat, A. Raafik, S. Le Vot, M. C. Devendrachari, A. R. Kottaichamy, N. C. Dargily, R. Thimmappa, O. Fontaine, M. O. Thotiyl, *J. Phys. Chem. Lett.* **2021**, *12*, 1374.

[29] D. Zhang, Q. Cai, O. O. Taiwo, V. Yufit, N. P. Brandon, S. Gu, *Electrochim. Acta* **2018**, *283*, 1806.

[30] X. Ma, H. Zhang, F. Xing, *Electrochim. Acta* **2011**, *58*, 238.

[31] B. Turker, S. Arroyo Klein, E.-M. Hammer, B. Lenz, L. Komsiyska, *Energy Convers. Manag.* **2013**, *66*, 26.

[32] F. Sepehr, S. J. Paddison, *Chem. Phys. Lett.* **2016**, *645*, 20.

[33] M. Li, T. Hikihara, *IEICE Trans. Fundam. Electron. Commun. Comput. Sci.* **2008**, *E91.A*, 1741.

[34] X. L. Zhou, T. S. Zhao, L. An, Y. K. Zeng, X. H. Yan, *Appl. Energy* **2015**, *158*, 157.

[35] R. P. Fornari, P. de Silva, *Wiley Interdiscip. Rev. Comput. Mol. Sci.* **2021**, *11*, e1495.

[36] S. Er, C. Suh, M. P. Marshak, A. Aspuru-Guzik, *Chem. Sci.* **2015**, *6*, 885.

[37] Y. Ding, G. Yu, *Chem* **2017**, *3*, 917.

[38] X. Li, *Electrochim. Acta* **2015**, *170*, 98.

[39] D. Zhang, A. Forner-Cuenca, O. O. Taiwo, V. Yufit, F. R. Brushett, N. P. Brandon, S. Gu, Q. Cai, *J. Power Sources* **2020**, *447*, 227249.

[40] Z. Shuai, H. Geng, W. Xu, Y. Liao, J. M. André, *Chem. Soc. Rev.* **2014**, *43*, 2662.

[41] R. N. Methekar, P. W. C. Northrop, K. Chen, R. D. Braatz, V. R. Subramanian, *J. Electrochem. Soc.* **2011**, *158*, A363.

[42] C. Health Turner, Z. Zhang, L. D. Gelb, B. I. Dunlapc, *Rev. Comput. Chem.* **2015**, *28*, 175.

[43] M. Andersen, C. Panosetti, K. Reuter, *Front. Chem.* **2019**, *7*, 202.

[44] A. U. Modak, M. T. Lusk, *Solid State Ionics* **2005**, *176*, 2181.

[45] G. Blanquer, Y. Yin, M. A. Quiroga, A. A. Franco, *J. Electrochem. Soc.* **2016**, *163*, A329.

[46] M. A. Quiroga, A. A. Franco, *J. Electrochem. Soc.* **2015**, *162*, E73.

[47] M. EL-Adawy, T. Paillat, G. Touchard, J. M. Cabaleiro, *IEEE Trans. Dielectr. Electr. Insul.* **2011**, *18*, 1463.

[48] J. W. Yan, Z. Q. Tian, B. W. Mao, *Curr. Opin. Electrochem.* **2017**, *4*, 105.

[49] J. P. Valleau, G. M. Torrie, *J. Chem. Phys.* **1982**, *76*, 4623.

[50] A. A. Franco, P. Schott, C. Jallut, B. Maschke, *J. Electrochem. Soc.* **2006**, *153*, A1053.

[51] P. Virtanen, R. Gommers, T. E. Oliphant, M. Haberland, T. Reddy, D. Cournapeau, E. Burovski, P. Peterson, W. Weckesser, J. Bright, S. J. van der Walt, M. Brett, J. Wilson, K. J. Millman, N. Mayorov, A. R. J. Nelson, E. Jones, R. Kern, E. Larson, C. J. Carey, İ. Polat, Y. Feng, E. W. Moore, J. VanderPlas, D. Laxalde, J. Perktold, R. Cimrman, I. Henriksen, E. A. Quintero, C. R. Harris, et al., *Nat. Methods* **2020**, *17*, 261.

[52] B. Andreaus, M. Eikerling, *J. Electroanal. Chem.* **2007**, *607*, 121.

[53] N. B. Luque, H. Ibach, K. Pötting, W. Schmickler, *Electrochim. Acta* **2010**, *55*, 5411.

[54] T. Liu, X. Wei, Z. Nie, V. L. Sprenkle, W. Wang, *Adv. Energy Mater.* **2016**, *6*, 1501449.

[55] R. A. Marcus, *J. Chem. Phys.* **1956**, *24*, 966.

[56] R. A. Marcus, *Angew. Chem.,–Int. Ed. Eng.* **1993**, *32*, 1111.

[57] M. A. Quiroga, K.-H. Xue, T.-K. Nguyen, M. Tułodziecki, H. Huang, A. A. Franco, *J. Electrochem. Soc.* **2014**, *161*, E3302.

[58] M. A. Quiroga, K. Malek, A. A. Franco, *J. Electrochem. Soc.* **2016**, *163*, F59.

[59] R. E. Bangle, J. Schneider, E. J. Piechota, L. Troian-Gautier, G. J. Meyer, *J. Am. Chem. Soc.* **2020**, *142*, 674.

[60] S. Ghosh, S. Horvath, A. V. Soudackov, S. Hammes-Schiffer, *J. Chem. Theory Comput.* **2014**, *10*, 2091.

[61] Y. Shao, Z. Gan, E. Epifanovsky, A. T. B. Gilbert, M. Wormit, J. Kussmann, A. W. Lange, A. Behn, J. Deng, X. Feng, D. Ghosh, M. Goldey, P. R. Horn, L. D. Jacobson, I. Kaliman, R. Z. Khaliullin, T. Kuś, A. Landau, J. Liu, E. I. Proynov, Y. M. Rhee, R. M. Richard, M. A. Rohrdanz, R. P. Steele, E. J. Sundstrom, H. L. Woodcock III, P. M. Zimmerman, D. Zuev, B. Albrecht, E. Alguire, et al., *Mol. Phys.* **2015**, *113*, 184.

[62] M. Cossi, N. Rega, G. Scalmani, V. Barone, *J. Comput. Chem.* **2003**, *24*, 669.

[63] A. Peyman, C. Gabriel, E. H. Grant, *Bioelectromagnetics* **2007**, *28*, 264.

[64] L. F. Hernández-Martínez, M. A. Chávez-Navarro, E. González-Tovar, M. Chávez-Páez, *J. Chem. Phys.* **2018**, *149*, 164905.

[65] P. M. S. Monk, R. D. Fairweather, M. D. Ingram, J. A. Duffy, *J. Chem. Soc., Perkin Trans.* **1992**, *2*, 2039.

[66] P. Neta, M.-C. Richoux, A. Harriman, *J. Chem. Soc., Faraday Trans. 2* **1985**, *81*, 1427.

[67] Q. Wu, T. Van Voorhis, *Phys. Rev. A* **2005**, *72*, 24502.

[68] S. Y. Mashayak, N. R. Aluru, *J. Chem. Phys.* **2018**, *148*, 214102.